

# Charge Transport in a Mixed Ionically/Electronically Conducting, Cationic, Polyacetylene Ionomer between Ion-Blocking Electrodes

Calvin H. W. Cheng, Fuding Lin, and Mark C. Lonergan\*

Department of Chemistry, The Materials Science Institute, Oregon Nanoscience and Microtechnologies Institute, University of Oregon, Eugene, Oregon 97403

Received: January 31, 2005

The electrical behavior of the cationic, polyacetylene-based, conjugated ionomer, poly[(2-cyclooctatetraenylethyl)trimethylammonium trifluoromethanesulfonate], sandwiched between gold electrodes is reported. The steady-state current of this mixed ionically/electronically conducting system is assigned to be unipolar diffusive hole transport for voltages below  $\sim 1.4$  V, giving way to bipolar migratory transport above  $\sim 1.4$  V. In the low-voltage regime, a non-Faradaically controlled doping model is proposed where p-doping at the anode is balanced by the charging of an ionic double layer at the cathode. In the high-voltage regime, n- and p-type regions extend from the electrodes as the voltage becomes sufficient to drive disproportionation and the electric field required by the redistribution of ions begins to substantially influence carrier transport. The assignment of a transport mechanism is primarily based on analyzing the decay of the steady-state system under short-circuit and open-circuit conditions. First, it is shown that the power describing the power-law decay of the short-circuit current is characteristic of the steady-state carrier profile. Second, it is argued that a component of the time-dependent, open-circuit voltage decaying more rapidly than the time scale for ion motion is indicative of a substantial migratory component to steady-state transport, as observed in the high-voltage regime. The hole and electron mobilities are estimated to be on the order of  $10^{-7}$ – $10^{-6}$   $\text{cm}^2 \text{V}^{-1} \text{s}^{-1}$ .

## Introduction

Polymeric mixed ionic-electronic conductors (MIECs) are being intensely investigated for potential application in solid-state lighting,<sup>1–7</sup> photovoltaics,<sup>8</sup> thin-film<sup>9</sup> and electrochemical transistors,<sup>10–13</sup> and memory devices.<sup>14,15</sup> The application of bias to MIECs can result in substantial changes in the electrical properties of the material due to the redistribution of ions. This redistribution makes possible substantial changes in the density and spatial distribution of doped sites relative to that in the unperturbed material, leading to properties not possible with pure electronic conductors. For instance, the ability to switch conduction pathways via voltage-induced changes in the doping level of polymeric MIECs have been exploited in developing electrochemical transistors,<sup>10–13</sup> as well as approaches to current rectification<sup>16</sup> and charge trapping.<sup>17–21</sup> The behavior observed in such systems is understood by considering the reversible formation and removal of electronically conducting regions. The active material is contacted by an ion-blocking electrode and an electrolyte, and the mixed ionic/electronic nature is mainly important in supporting electrochemical oxidation and reduction to alter a uniform doping level. More complex and voltage-dependent spatial variations in ion, electron, and hole densities arise in polymeric MIECs sandwiched between two ion-blocking electrodes, as is the focus of this paper. Single-layer polymer light-emitting electrochemical cells are an example of such a system where low operating voltages, relative to their purely electronic counterparts, result from the mixed ionic/electronic nature of the active material.<sup>1–7</sup> Understanding the connectedness of the ionic and electronic processes in MIECs between blocking electrodes is an important step in optimizing and

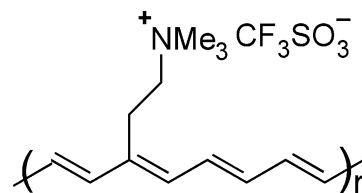


**Figure 1.** Poly[(2-cyclooctatetraenylethyl)trimethylammonium trifluoromethanesulfonate] ( $P_C$ ).

guiding the development of polymer light-emitting electrochemical cells as well as other types of devices based on these materials.

The goal of this paper is to characterize and describe the charge transport properties of the polyacetylene-based ionomer ( $P_C$ )<sup>22,23</sup> shown in Figure 1 when contacted with ion-blocking gold electrodes. All of the reported studies are on the initially undoped material. Characterization of the steady state is emphasized, although a number of transient measurements are used in this characterization. The work endeavors to elucidate the carrier and anion distributions, the nature of the transport processes (e.g., migratory versus diffusive, unipolar versus bipolar), and any electrode limitations, all as a function of applied bias.

The polymer  $P_C$  is an ideal material for the fundamental study of conjugated polymer MIECs. Unlike the more widely studied blends of conjugated polymers and polymer electrolytes,<sup>1–7</sup> it is a single-component system. It is also a member of a larger family of conjugated ionomers that provide for control over ion type and density. Furthermore, understanding transport in this family of MIECs is essential to elucidating recently observed phenomena based on these materials: for instance, steady-state, unidirectional electron transport through a bilayer structure of  $P_C$  and an anionically functionalized analogue<sup>24</sup> or the subse-

\* lonergan@uoregon.edu.

quent use of this bilayer as a stepping stone to a conjugated polymer pn junction.<sup>25</sup>

## Experimental Methods

**Materials.** Dimethyl sulfoxide (DMSO) and anhydrous tetrahydrofuran (THF) were purchased from Aldrich. The anhydrous THF was used as received. DMSO was distilled over calcium hydride, then run through two freeze–pump–thaw degas cycles. The predominantly trans form of poly[(2-cyclo-octatetraenylethyl)trimethylammonium trifluoromethanesulfonate] was available from a previous study.<sup>26</sup> Deposition solutions were made by dissolving PC in DMSO.

**Sample Preparation.** The Au | PC | Au structures studied were prepared on glass-slide substrates. The glass slides were cleaned by soaking in concentrated HCl for at least 4 h, followed by a thorough rinsing in deionized water. Bottom gold electrodes were prepared by sequential thermal evaporation of Cr (1.5 nm) then Au (10 nm) onto the glass slides. The electrode area was defined using a physical evaporation mask to be  $A = 0.12 \text{ cm}^2$ . Polymer films were then deposited onto the gold electrodes by spin-coating from a  $20 \text{ mg mL}^{-1}$  solution. A  $100\text{-}\mu\text{L}$  volume of solution was applied to a substrate spinning at 200 rpm where the solution was spread out evenly to cover the electrode area. When the desired area was covered with solution, the spinning rate was increased to 700 rpm, and the sample was spun for 40 min. Polymer solutions were filtered through a  $0.2\text{-}\mu\text{m}$  Teflon filter prior to spin-coating. The film thickness could be increased by slowing the spin rate. The polymer film thickness ( $l$ ) was varied between 100 and 3000 nm as measured by a Dektak 6 ST profilometer. After spin-coating, films were placed under vacuum (20 mTorr) for at least 1 h. To complete the sandwich structure, a top 10-nm-thick gold electrode was thermally evaporated onto the polymer film. Electrical contacts to the electrodes were made by silver-printing a tinned copper wire to contact pads of the metal films. All films were stored under vacuum (20 mTorr) for several hours after thermal evaporation of the top contact before usage. All experiments were performed under vacuum on initially undoped films.

**Electrical Measurements.** Controlled-potential electrical measurements were performed using the analogue interface of a Solartron 1287 potentiostat and a National Instruments BNC-1110 digital-analogue converter (DAC). The system was controlled and measurements were collected using a custom Labview program. For time-dependent experiments, the time base was provided by the measurement frequency of the DAC. Current density–voltage ( $J$ – $V_{\text{app}}$ ) measurements were performed using scan rates between  $10^{-3}$  and  $10^3 \text{ V s}^{-1}$ . For voltage step experiments, a constant voltage  $V_0$  was applied until the measured current became constant for at least 30 s. Transient  $J$ – $V_{\text{app}}$  measurements of the steady-state condition were performed by sweeping the voltage at  $1000 \text{ V s}^{-1}$  over the range  $\pm 3 \text{ V}$  after steady state had been achieved at each  $V_0$ . Open-circuit voltage and current decay profiles were measured by first bringing the system to steady state at a particular  $V_0$  and then switching the system from the potentiostat to either a high-impedance (open-circuit) National Instruments DAC or a low-impedance (short-circuit) Kiethley 485 picoammeter.

**UV–vis Absorbance.** UV–vis spectra over the range 400–900 nm were recorded simultaneously with the electrical measurements. Spectra were recorded every 10 s using a USB2000 spectrometer,  $200\text{-}\mu\text{m}$  optical fibers, and a tungsten light source, all from Ocean Optics, Inc. The absorption spectrum is fairly sensitive to chemical changes in the polymer system,<sup>27</sup> but because of the high absorptivity of the Au | PC |

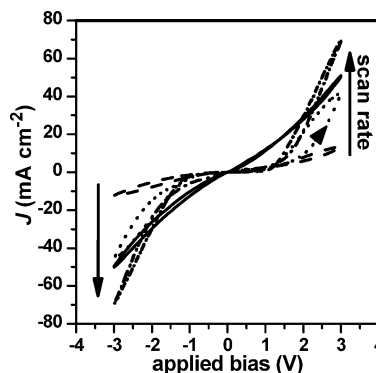


**Figure 2.** Current density–voltage ( $J$ – $V_{\text{app}}$ ) behavior as a function of scan rate:  $0.01$  (•••),  $0.1$  (---),  $1$  (-.-), and  $10$  (—)  $\text{V s}^{-1}$  (PC2,  $l = 320 \text{ nm}$ ). Vertical arrows indicate the direction in which the magnitude of the sweep rate decreases. The  $10 \text{ V s}^{-1}$  sweep is enlarged by a factor of 5 for clarity. The arrow on the  $0.1 \text{ V s}^{-1}$  curve indicates the direction of the forward sweep.

Au structure, only qualitative statements about chemical changes can be made.

## Results

A variety of measurements were performed on more than twelve separate films of varying film thickness. The qualitative behavior of all the films was the same, but the currents measured for films of similar thickness in response to identical electrical stimuli could vary at the extreme by a factor of 5. Most of the results shown in this section are for a representative film (PC1) of thickness 300 nm and include characterization of the steady state and the decay of the steady state. The data for this film are used in the discussion for further calculation with parameters expressed to a single significant figure owing to the film-to-film reproducibility. These results are complemented by thickness-dependent measurements of the steady-state current on a range of films, as well as measurements on three additional films of thicknesses between 300 and 350 nm (PC2, PC3, and PC4) that were conducted to higher applied biases than PC1. These latter experiments were carried out on separate films, because they involved applying biases of greater than 3 V for periods of minutes. The resulting currents were in excess of  $20 \text{ mA cm}^{-2}$  and resulted in some irreversible degradation of electrical characteristics.

The interplay between ionic and electronic processes in the mixed ionic/electronic conducting Au | PC | Au system was first investigated using  $J$ – $V_{\text{app}}$  measurements as a function of scan rate. Figure 2 shows the  $J$ – $V_{\text{app}}$  behavior at several scan rates for PC2 film of thickness  $l = 320 \text{ nm}$ . Over the examined voltage range and above a scan rate of  $10 \text{ V s}^{-1}$ , the  $J$ – $V_{\text{app}}$  characteristics were observed to be nearly linear. Changing the polymer film thickness in the range of 100 to 3000 nm did not alter the linear response observed at  $1000 \text{ V s}^{-1}$ , and the apparent conductivity ( $\sigma_a = l(dJ/dV_{\text{app}})$ ) of the film was roughly independent of film thickness. Experiments after those reported herein also demonstrated that heating of the samples under vacuum diminished  $\sigma_a$ . Slowing the sweep rate to less than  $10 \text{ V s}^{-1}$  resulted in the  $J$ – $V_{\text{app}}$  characteristics becoming increasingly nonlinear with the current diminished for  $|V_{\text{app}}| < 1$  and enhanced for  $|V_{\text{app}}| > 1 \text{ V}$  relative to the fast scan rate result. Films swollen with solvent were also characterized in an effort to potentially alter the ion diffusivity. Swelling a film with  $\text{CH}_3\text{-CN}$  through the porous top gold contact preserved linear response at fast scan rates, but  $\sigma_a$  increased by a factor of 3. In the swelled film, nonlinear  $J$ – $V_{\text{app}}$  behavior was observed for

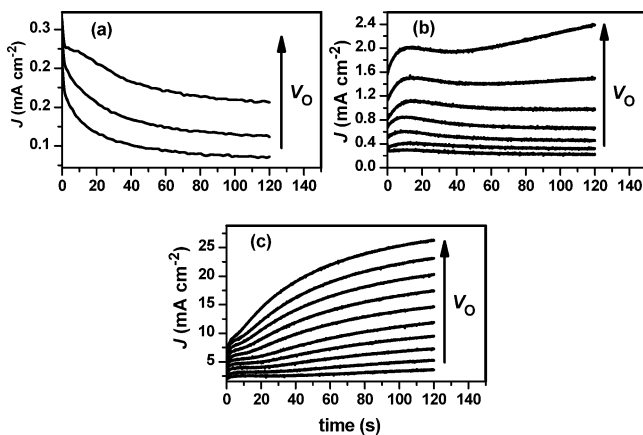


**Figure 3.** Current transients for potential-step experiments as a function of  $V_0$  (PC1,  $l = 300$  nm). The transients show the time-dependent current density ( $J$ ) in response to a potential step  $V_0$  and are separated into three regions: (a)  $0.6 \leq V_0 \leq 0.8$  V, (b)  $0.9 \leq V_0 \leq 1.5$  V, (c)  $1.6 \leq V_0 \leq 2.5$  V. The potential-step experiments span the indicated voltage ranges in increments of 0.1 V.

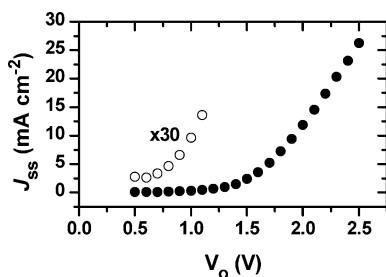


**Figure 4.** Steady-state current density  $J_{ss}$  (solid circles) as a function of voltage  $V_0$  (PC1,  $l = 300$  nm). The low-voltage data is expanded by a factor of 30 (open circles).

scan rates of  $100 \text{ V s}^{-1}$  or less, with significantly more hysteresis.

Potential-step experiments were performed to separate the temporal and voltage dependencies more clearly than the  $J$ - $V_{app}$  experiments of Figure 2. The chronoamperograms recorded in response to various potential steps,  $V_0$ 's, are shown in Figure 3 for PC1 film ( $l = 300$  nm). As separated in Figure 3, three regimes of behavior were observed corresponding to the voltage ranges: low ( $0 < V_0 < 0.8$  V), intermediate ( $0.8 < V_0 < 1.2$  V), and high ( $V_0 > 1.2$  V). Stepping the potential in the low-voltage regime resulted in a current transient that gradually decreased to a steady-state value.<sup>28</sup> Stepping the potential in the high-voltage regime resulted in current transients that increased to a slight plateau followed by a significantly larger increase. Stepping the potential in the intermediate regime resulted in a combination of the behaviors observed in the high and low regimes. In all cases studied, steady state was achieved after 5 min. Figure 4 shows the steady-state current density ( $J_{ss}$ ) as a function of  $V_0$ . Neither power-law nor exponential fits adequately described the full range of the nonlinear data. The  $J_{ss}$  was observed to decrease with increasing film thickness, as shown in Figure 5 for two values of  $V_0$ . The large scatter in the data of Figure 5 gives an idea of the film-to-film reproducibility and makes it difficult to quantify the precise form of the thickness dependence. It does appear, however, that  $J_{ss}$  depends more strongly on film thickness at the lower voltage.

The amount and nature of charge stored in the polymer film at steady state was investigated by studying the relaxation of the system from steady state to equilibrium using two methods. In the first method, the system was short-circuited through a low-impedance ammeter after reaching steady state, and the

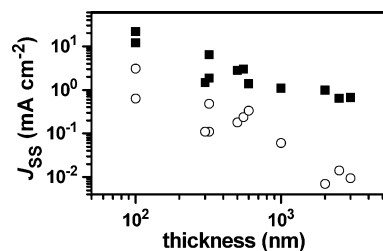


**Figure 5.** Thickness dependence of the steady-state current at  $V_0 = 0.6$  V (open circles) and  $V_0 = 1.4$  V (solid squares).

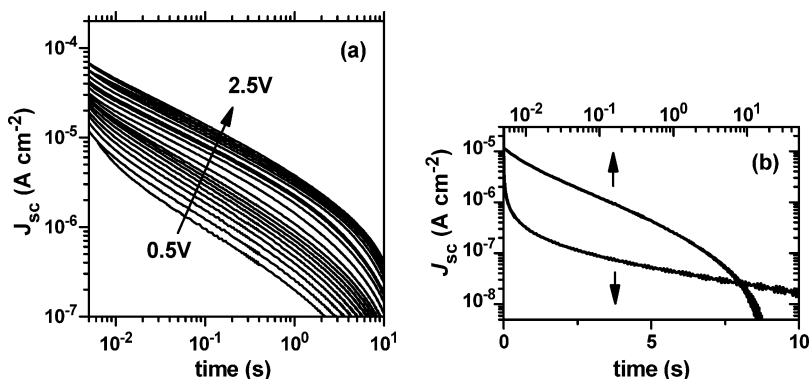
resulting current density ( $J_{sc}$ ) transient recorded. In the second, the system was switched from an applied bias to an open-circuit condition, and the resulting open-circuit voltage ( $V_{oc}$ ) transient recorded with a high-impedance voltmeter.

Figure 6 shows short-circuit transients for the relaxation of film PC1 from steady state as a function of  $V_0$ . After switching to a low-impedance ammeter, the  $J_{sc}$  decayed to 95% of its initial current within 0.1 s. All of the decays were first characterized by a power-law dependence giving way to exponential behavior at longer times, as shown in Figure 6b. In the low-voltage regime, the power-law decay was characterized by an exponent of magnitude  $a = |d(\log J_{sc})/d(\log t)|$  approximately equal to 0.65 transitioning to near 0.5 in the high-voltage regime, as shown in Figure 7. The variation in the time constant describing the exponential decay was less than 5% over the range 0.5–2.0 V, where its average value was 3.9 s. Above 2 V, the time constant increased more sharply to a value of 4.8 s at 2.5 V.

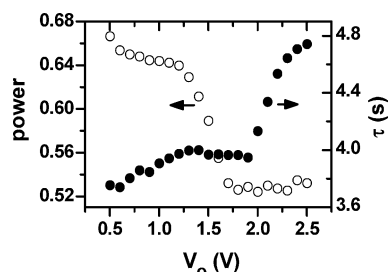
The  $J_{sc}$  decays were integrated to determine the charge,  $Q_{sc}$ , passing through the external short circuit during the relaxation process for each value of  $V_0$ . A clear transition in the voltage dependence of  $Q_{sc}$  was observed at  $V_0 = 1.5$  V (Figure 8). On both sides of this transition voltage,  $Q_{sc}$  responded linearly to  $V_0$ , but the dependence was approximately 4 times as strong above  $V_0 = 1.5$  V as below it. A linear fit to the data in the low-voltage regime, including the point (0,0), resulted in an apparent capacitance of  $3.5 \mu\text{F cm}^{-2}$ .

Figure 9 shows several open-circuit voltage transients over the different regimes of  $V_0$ . The earliest time  $V_{oc}$  measured was collected at 1.4 ms and is termed  $V_{oc}^0$ . In the low-voltage regime,  $V_{oc}$  decayed exponentially from  $V_0 = V_{oc}^0$  with the time constant for the decay increasing with  $V_0$ . At high  $V_0$ , a component of the applied voltage decayed before  $V_{oc}^0$  was measured. The subsequent decay from  $V_{oc}^0$  was slower than in the low-voltage regime, with  $V_{oc}(t)$  remaining nearly constant for approximately 20 s and then decaying nearly linearly at the highest voltages studied.

The steady state was also characterized by transient  $J$ - $V_{app}$  measurements. Fast ( $1000 \text{ V s}^{-1}$ )  $J$ - $V_{app}$  curves were collected immediately after equilibrating the system at a particular  $V_0$ . Increasing  $V_0$  from zero changed the transient  $J$ - $V_{app}$  behavior from linear to rectifying, as shown in Figure 10. For rectifying curves, the forward bias current was not observed to increase exponentially as is typical for diodes. Rather, it increased linearly past some threshold or turn-on voltage. The rectification ratio,  $RR = J(V_{app})/J(-V_{app})$ , was observed to reach a value of 30 at 3 V. All of the curves relaxed to the same equilibrium, linear  $1000 \text{ V s}^{-1}$   $J$ - $V_{app}$  behavior (as in Figure 2 or Figure 10 for  $V_0 = 0$ ) within several minutes. Changing the sign of  $V_0$  had no effect, except for changing the direction of the transient rectification. The fast  $J$ - $V_{app}$  measurements also provided a measure of  $V_{oc}^0$  as the voltage where  $J$  crosses zero. These  $V_{oc}^0$  values as a function of  $V_0$  for film PC1 are shown in Figure 11.



**Figure 6.** (a) Short-circuit current density ( $J_{sc}$ ) as a function of time for steady states arrived at by driving with various voltages  $V_o$  (PC1,  $l = 300$  nm). The  $J_{ss}$  is measured by shorting the steady-state system through a low-impedance ammeter. The plot is a log–log representation. The various decays are in 0.1 V increments and shift systematically in the direction shown over the voltage range 0.5–2.5 V. (b) Comparison of log–log and semilog plots for  $V_o = 0.6$  V.



**Figure 7.** Power extracted (left ordinate) over the range 0.01–1 s from a power-law fit to and time constant (right ordinate) extracted over the range  $t = 2.5$ –7.5 s from an exponential fit to  $J_{sc}$  vs time as a function of  $V_o$  (PC1,  $l = 300$  nm).

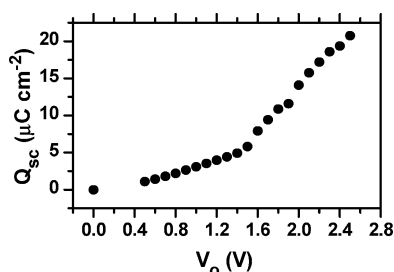


**Figure 8.** Charge  $Q_{sc}$  (solid circles) extracted upon short-circuiting various steady states through an external low-impedance ammeter (PC1,  $l = 300$  nm). The various points are the integrals of the traces in Figure 6, each corresponding to a steady state arrived at by driving with voltage  $V_o$ .

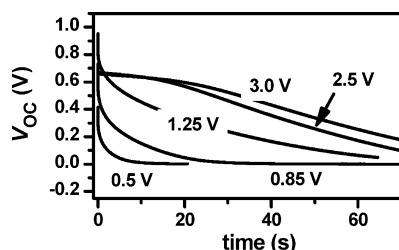


**Figure 9.** Open-circuit voltage ( $V_{oc}$ ) as a function of time for the decay of steady states arrived at by driving with various voltages  $V_o$ 's as labeled (PC4,  $l = 300$  nm). The  $V_{oc}$  is measured by open-circuiting the steady-state system across a high-impedance voltmeter.

Electronic absorption spectroscopy was performed to monitor electrochemical changes in the polymer backbone upon application of a potential step. For  $V_o < 2.0$  V applied over periods up to 30 min, no change in the absorbance spectrum was noted. At higher  $V_o$ , a bleach in the  $\pi$ – $\pi^*$  absorption ( $\sim 600$  nm) and an increase in the absorbance above 800 nm was observed, as

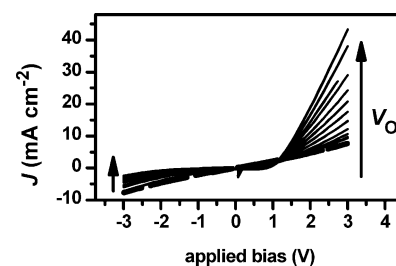


**Figure 10.** Transient  $J$ – $V_{app}$  behavior characterizing steady states arrived at by driving with various voltages  $V_o$ 's for two minutes (PC1,  $l = 300$  nm). The transient curves were collected at  $1000 \text{ V s}^{-1}$  immediately following the two-minute drive period. The arrows show the direction of increasing  $V_o$  stepped in 0.1 V increments from 0.3 to 1.5 V. As  $V_o$  increases, the transient curves become increasingly asymmetric.

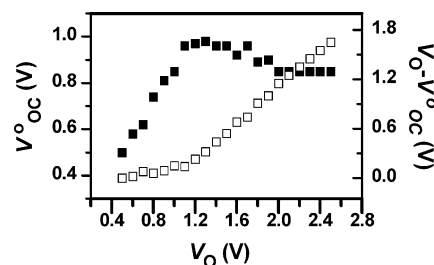


**Figure 11.**  $V_{oc}^o$  (black squares, left axis) and  $V_o - V_{oc}^o$  (open squares, right axis) as a function of  $V_o$  (PC1,  $l = 300$  nm).

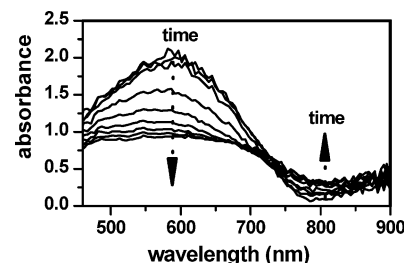


**Figure 12.** Time-dependent UV–vis absorption spectra for a film held at 3 V (PC3,  $l = 350$  nm). The scans are in two-minute intervals.

shown in Figure 12 for film PC3 ( $l = 350$  nm). The spectrum in Figure 12 continued to evolve for periods greater than 30 min, although with some loss of reversibility at the longer drive times. The magnitude of the bleach at a given time increased with increasing  $V_o$  above 2.0 V.

Thermal evaporation of other metals onto the polymer film was used in an attempt to explore any dependence on the



electrode work function. Evaporation of Al, Zn, or Ca followed by application of a voltage appeared to cause what is believed to be an irreversible metal oxidation at the polymer–metal interface. This reaction was evident from the  $J$ – $V_{\text{app}}$  behavior of the Au | P<sub>C</sub> | M structures. The initial sweep of the voltage resulted in strongly asymmetric  $J$ – $V_{\text{app}}$  behavior. Subsequent sweeps, however, showed very little current. Chromium was evaporated onto the polymer film with no sign of chemical change to the polymer; the  $J$ – $V_{\text{app}}$  behavior of the Cr | P<sub>C</sub> | Cr structure showed no significant differences from Au | P<sub>C</sub> | Au structures.

## Discussion

The experimental results of this work are reminiscent of the  $J$ – $V_{\text{app}}$  characteristics observed in other polymer MIECs.<sup>2,3,7</sup> Several models have been proposed to explain the steady-state  $J$ – $V_{\text{app}}$  characteristics of these polymer MIECs.<sup>1,29–39</sup> Herein, the transport in the Au | P<sub>C</sub> | Au system will be discussed within a predominately electrochemical framework, and the motion of electrons, holes, and anions considered as quasi-free particles using the macroscopic Nernst–Planck equation. The polymer is considered to have a series of discrete redox sites that can be in any one of three oxidation states: +1 (p-type), 0 (undoped, u), or –1 (n-type). They are described by densities  $n_p(x, t)$ ,  $n_u(x, t)$ , and  $n_n(x, t)$ , respectively, that can vary with position  $x$  across the film if not at equilibrium or steady-state with time  $t$ . The anode position is taken as  $x = 0$  and the cathode as  $x = l$ . Separate three-electrode, cyclic voltammetry experiments indicate a total density  $n_{\text{tot}} = n_p(x, t) + n_u(x, t) + n_n(x, t)$  of  $\sim 0.5 \times 10^{21} \text{ cm}^{-3}$ .<sup>23</sup> For comparison, the stoichiometric anion density in P<sub>C</sub> is  $n_A^0 = 1.8 \times 10^{21} \text{ cm}^{-3}$ . Voltammetry also indicates that the energy distribution of sites is somewhat broader than given by the Nernst equation

$$E = E_{\text{O/R}}^0 - \frac{k_B T}{\zeta q} \ln \frac{n_R}{n_O} \quad (1)$$

with  $\zeta = 1$ , and where  $q$  is the elementary charge,  $k_B$  the Boltzmann constant,  $T$  the temperature,  $E$  the electrode potential (in volts),  $E_{\text{O/R}}^0$  the standard potential for the reduction of O to R, and  $n_O$  and  $n_R$  are the densities of O and R, respectively. The apparent standard reduction potentials for p- and n-doping P<sub>C</sub> are  $E_{\text{p/u}}^0 = 0.4 \text{ V}$  versus SCE ( $\sim 5.1 \text{ V}$  vs vac) and  $E_{\text{u/n}}^0 = -1.0 \text{ V}$  versus SCE ( $\sim 3.7 \text{ V}$  vs vac), respectively.

The remainder of this discussion is divided into four sections. The first deals with a qualitative discussion of the scan-rate-dependent  $J$ – $V_{\text{app}}$  behavior and assignment of ionic conductivity. A more detailed analysis of the steady state is then presented in the middle two sections, which are separated into the low- and high-voltage regimes, as suggested by the experimental data, and roughly divided by  $V_0 = 1.3$ – $1.4 \text{ V}$ . Finally, the ideas developed in the discussion of the steady state are used to qualitatively discuss the chronoamperograms describing the approach to steady state in response to a potential step.

**Scan-Rate-Dependent  $J$ – $V_{\text{app}}$  Behavior.** The interplay between ionic motion, charge injection, and transport in P<sub>C</sub> is illustrated by the scan-rate dependence of the  $J$ – $V_{\text{app}}$  curves. The fast  $J$ – $V_{\text{app}}$  curves are assigned to the ionic conductivity of the system in the kilohertz regime. The assignment to ionic conductivity comes primarily from the ohmic behavior, the decrease in the current with increasing  $l$ , and the increase in  $\sigma_a$  observed upon swelling with solvent. The decay of the current following a low-voltage potential step is also consistent with the current at short times being predominately due to ionic motion and diminishing with time because of polarization at

the ion-blocking gold electrodes. The decay of this current also demonstrates that the fast scan-rate behavior is not dominated by metallic shorts.

The ionic conductivity calculated from the  $1000 \text{ V s}^{-1}$   $J$ – $V_{\text{app}}$  curve for film PC1 is  $2 \times 10^{-8} \text{ S cm}^{-1}$  and in the range  $10^{-8}$ – $10^{-7} \text{ S cm}^{-1}$  for all of the samples studied at room temperature. This conductivity is comparable to that observed for single-ion conduction in solid-state polyelectrolytes such as polyphosphazenes<sup>40,41</sup> and poly(tetraalkoxyaluminates)<sup>42</sup> and a couple of orders of magnitude lower than prototypical polyether-based polymer electrolytes.<sup>43–46</sup> The conductivity is perhaps surprisingly high given that P<sub>C</sub> is well below its glass transition temperature at room temperature. Classic polymer electrolytes typically exhibit substantial ionic conductivity only above their glass transition temperatures. As mentioned earlier, studies after those presented herein demonstrate that the apparent ionic conductivity decreases as the sample is heated under vacuum. This suggests that the specific films studied herein still contain some residual DMSO, which may be responsible for the higher than expected conductivity.

The transition to nonlinear behavior upon slowing the scan rate is primarily a consequence of the ion-blocking electrodes. These prevent ionic conduction from contributing at the steady state and for the substantial accumulation of ions at the P<sub>C</sub> | Au interface. The latter creates a large potential drop at the electrode surface that can drive the injection of electronic charges and the doping of the polymer film. Qualitatively, the reduction of current in the low-voltage portion of the  $J$ – $V_{\text{app}}$  behavior with decreasing scan rate is due to the ionic current falling out, while the rise in the current in the high-voltage portion is due to an increase in the electronic conductivity of the sample due to doping.<sup>2,3</sup> For the remainder of the discussion, we focus on the behavior at very slow scan rates, in other words, the steady-state behavior. The simultaneous evolution of both time and potential in sweep methods complicates their analysis, and a quantitative treatment is beyond the scope of this paper.

**Steady State, Low-Voltage Regime.** The steady state in the low-voltage regime is characterized by the following observations: (1)  $J_{\text{ss}}$  decreases as  $l$  increases; (2)  $V_{\text{oc}}^0$  is approximately equal to  $V_0$ ; (3)  $Q_{\text{sc}}$  increases linearly with  $V_0$ ; (4)  $J_{\text{sc}}$  decays from steady state initially following a power law with  $a \approx 0.65$  and then exponentially; (5)  $J_{\text{ss}}$  increases nonlinearly with voltage, increasing, for example, by approximately a factor of 4 upon doubling  $V_0$  from 0.5 to 1.0 V. Each of the above observations provides insight into the steady state of P<sub>C</sub> under applied bias as discussed below.

The dependence of  $J_{\text{ss}}$  on  $l$  suggests that it derives from processes within the P<sub>C</sub> film, rather than from heterogeneous charge transfer kinetics at the Au | P<sub>C</sub> interface. Interfacial charge transfer rates between a metal and a molecular system strongly depend on the electric field ( $F$ ) at the interface.<sup>47</sup> The electrostatic potential developed across a metal | MIEC | metal system upon application of bias drops primarily across ionic double layers formed at the electrode interfaces, as long as the bias does not too strongly perturb the ion distribution.<sup>39,48</sup> The steady-state form of this double layer and consequently  $F$  at the interface depends on  $V_{\text{app}}$ , but not the thickness of the MIEC. The dependence of  $J_{\text{ss}}$  on  $l$  should be very weak if it is a measure of interfacial charge transfer kinetics. The observed dependence of  $J_{\text{ss}}$  on  $l$  indicates control by bulk processes within the P<sub>C</sub> film.<sup>49</sup> The electrodes can be considered ohmic or reversible to at least one if not both types of carriers at steady state. At a reversible electrode, the surface concentrations of the various

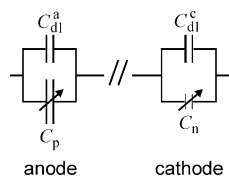


**Figure 13.** Schematic of the electrode charging capacitances where  $C_{dl}^a$  and  $C_{dl}^c$  are the weakly voltage-dependent double-layer charging capacitances at the anode and cathode, respectively, and  $C_p$  and  $C_n$  are the more strongly voltage-dependent differential capacitances describing charge storage in p- and n-type states, respectively. Near equilibrium for  $P_C$ ,  $C_p > C_{dl}^a \approx C_{dl}^c > C_n$  as schematically indicated.

oxidation states are determined by the electrode potential via the Nernst equation.<sup>47</sup>

The agreement between  $V_{oc}^o$  and  $V_o$  argues for purely diffusive transport.  $V_{oc}^o$  is measured on a time scale slower than the rearrangement of electronic carriers, but faster than the large-scale rearrangement of the ionic distribution. If a substantial portion of the electronic transport were driven by migration, the carriers involved would rapidly migrate to dissipate  $F$  upon removal of  $V_o$ . The component of  $V_o$  driving the migration of electrons and holes would decay before  $V_{oc}^o$  is measured. The agreement between  $V_{oc}^o$  and  $V_o$  in the low-voltage regime signals mainly diffusive transport. The applied bias drives the formation of a gradient in doped sites with the chemical potential drop across the film nearly equaling  $V_o$ .

The  $Q_{sc}$ – $V_o$  relation and the form of the decay of  $J_{sc}$  are particularly interesting. Before discussing their significance to the steady state of  $P_C$  under applied bias, the meaning of  $Q_{sc}$  must first be addressed. Upon short-circuiting, excess carriers injected into the polymer will dissipate either by recombination within the polymer, which is only possible in the case of bipolar injection, or at the metal electrodes. Any charges stored in the ionic double layers will also contribute. These decay processes can occur either with the passage of charges through the external short circuit or internally. Only the former will contribute to  $J_{sc}$ . Hence, the charge  $Q_{sc}$  extracted from integration of  $J_{sc}$  is a lower limit on the total charge stored within the film. The extent to which it is a lower limit depends on the branching ratio between the internal and external decay pathways. Below, it will be argued that in the low-voltage regime two-thirds of the total charge is extracted through the external pathway independent of voltage.

There are four primary sources where electronic charges can be stored in the Au |  $P_C$  | Au system: the charge stored in the double layers at the anode (a) and cathode (c),  $Q_{dl}^a$  and  $Q_{dl}^c$ , respectively, and the charge stored through p-type or n-type doping of the polymer film,  $Q_p$  and  $Q_n$ , respectively. Overall charge neutrality requires that  $Q_{dl}^a + Q_p = -(Q_{dl}^c + Q_n)$ .<sup>50</sup> The  $Q$ – $V_o$  relations for these various processes determine the overall  $Q$ – $V_o$  relation as well as the relative potential drops at the anode versus the cathode. Each process can be cast in terms of a voltage-dependent differential capacitance as shown in Figure 13. Over a given voltage increment, the larger of the capacitances at each electrode (elements in parallel) will dominate the charging characteristics of that electrode, with the overall charging behavior dominated by the smaller of the two net electrode capacitances (elements in series).

The observed linear  $Q_{sc}$ – $V_o$  relation is consistent with the charging of an ionic double layer, although some mild voltage dependence of the capacitance and, hence, nonlinearity might be expected. If governed by the doping process, a much stronger dependence of  $Q_{sc}$  on  $V_o$  would be expected. At low doping

levels such that  $n_i \approx n_{tot}$ ,<sup>51</sup> the surface concentration of doped sites at a reversible electrode increases exponentially with electrode potential as given by the Nernst equation. The resulting  $Q$ – $V$  relation would be expected to scale similarly leading to a strong dependence of the differential capacitance on voltage, in contrast to that observed.

The capacitance extracted from the low-voltage portion of Figure 8 and assuming that  $2/3$  of the total charge contributes to  $Q_{sc}$  (see below) is  $C_{dl} = 5 \mu F \text{ cm}^{-2}$ . The simple Gouy–Chapman model<sup>47</sup> of the ionic double layer predicts  $C_{dl}^{GC} = 75 \mu F \text{ cm}^{-2}$  in the limit of low surface potential and for  $\epsilon = 6.0 \epsilon_o$  and  $n_A = 1.8 \times 10^{21} \text{ cm}^{-3}$ . The  $C_{dl}^{GC}$  being higher than  $C_{dl}$  suggests that the free ion content in  $P_C$  is much less than the stoichiometric ion content because of strong ion pairing. The effective anion density back-calculated from  $C_{dl}$  and the Gouy–Chapman model is  $5 \times 10^{18} \text{ cm}^{-3}$ .

Although the  $Q_{sc}$ – $V_o$  relation is consistent with the charging of an ionic double layer, the decay of  $J_{sc}$  from steady state does not follow the form typical of such a process. The decay of a charged double layer in a purely ionically conducting system proceeds with an exponential  $J$ – $t$  relation governed by the  $R_1 C_{dl}$  time constant, with  $R_1$  the resistance of the ionic conductor. The exponential behavior results from predominantly migratory currents. In contrast to this behavior, a dominant component of the  $J_{sc}$ – $t$  relation for  $P_C$  follows a power law with  $a \approx 1/2$ . Such a form is more typical of diffusive behavior.<sup>47</sup> Diffusive decay would be expected for charges stored in doped states where the coupling of the ion and carrier fluxes will result in an ambipolar, diffusive process.

The paradox of the linear  $Q_{sc}$ – $V_o$  relation and  $a \approx 1/2$  is resolved by considering the situation where there is a strong imbalance between hole and electron injection. Such unipolar injection at low voltages has been previously proposed by several groups studying polymeric MIECs.<sup>1,9,35,36,52</sup> We propose a non-Faradaically controlled doping model of unipolar injection where doping at one electrode is coupled to the charging of an ionic double layer at the other. The Fermi level of gold is much closer to  $E_{p/n}^o$  than  $E_{u/n}^o$ . It is expected then that  $n_p(0, ss) \gg n_n(l, ss)$ , and hence,  $|Q_p| > |Q_n|$ . In this case, the p-type doping at the anode will have to be balanced predominantly by the non-Faradaic charging of the double layer at the cathode:  $|Q_p| \approx |Q_{dl}^c|$ . This can give rise to a situation where the charging of the system is governed by  $C_{dl}$ , but because the charging of this double layer is coupled to doping of the polymer at the complementary electrode, the decay of  $J_{sc}$  from steady state is diffusive.

The above discussion suggests a picture of the steady state as shown in Figure 14A, which is for the non-Faradaically controlled case with  $n_p(0, ss) \gg n_n(l, ss)$ . The density of n-doped sites is essentially negligible relative to the density of p-doped sites. As such, a nonzero  $n_p$  extends all the way from the anode to the cathode where an infinite recombination velocity is assumed such that  $n_p(l, t) = 0$ . The constant gradient in  $n_p$  reflects the absence of any substantial  $F$  within the bulk and negligible recombination. The crosshatched area represents the charge stored in p-doped sites, and this, along with a relatively small density of holes on the anode surface, is balanced by electrons on the cathode surface. The absolute anode potential is positioned such that a small change will result in a very large change in  $Q_p$ . Most of the potential will hence have to drop at the cathode to enable the much weaker  $Q$ – $V$  relation for double-layer charging to keep up.

The diffusive decay of the triangular  $n_p(x, ss)$  profile in Figure 14A under short-circuit conditions was analyzed for a more

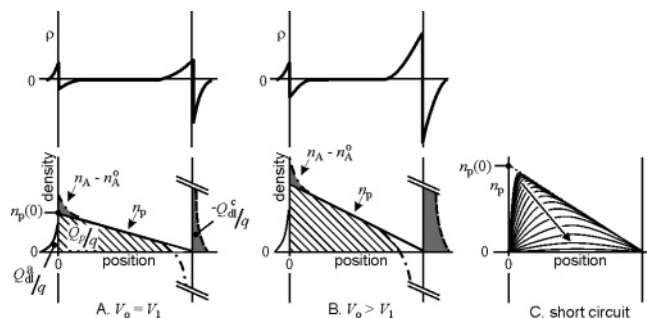


**Figure 14.** The excess charge density ( $\rho$ , top) and particle concentration (bottom) as a function of position within the Au | P<sub>C</sub> | Au structure within the low-voltage regime. The hole concentration is represented by  $n_p$ , whereas the anion concentration is expressed as the difference between  $n_A$  and  $n_A^0$ . (A) Steady-state picture of the non-Faradaically-controlled case at a voltage,  $V_1$ . A triangular concentration profile of holes (solid line) extends from the anode to the cathode, where an infinite recombination rate is assumed. The anion concentration profile (dash-dot line) essentially mirrors the hole profile except near the electrodes. (B) Steady-state picture at  $V_o > V_1$ . (C) Decay of  $\bar{n}_p(\bar{x}, \bar{t})$  from the steady state under short-circuit conditions. The concentration profiles are those from numerical solution of eqs 2 and 3. The arrow represents moving forward in time.

quantitative comparison to the experimental P<sub>C</sub> system. Fick's second law, written in reduced form

$$\frac{d\bar{n}_p(\bar{x}, \bar{t})}{d\bar{t}} = \frac{d^2\bar{n}_p(\bar{x}, \bar{t})}{d\bar{x}^2} \quad (2)$$

was solved numerically, subject to the following boundary conditions:

$$\begin{aligned} \bar{n}_p(\bar{x}, 0) &= 1 - \bar{x} \\ \bar{n}_p(\bar{x} = 1, \bar{t}) &= 0 \\ \bar{n}_p(0, \bar{t} > 0) &= 0 \end{aligned} \quad (3)$$

where  $\bar{n}_p(\bar{x}, \bar{t}) = n_p(\bar{x}, \bar{t})/n_p(0, 0)$ ,  $\bar{t} = tD_A/l^2$ , and  $\bar{x} = x/l$ . The anion diffusion coefficient,  $D_A$ , was assumed to be much smaller than the hole diffusion coefficient so that the ambipolar diffusion coefficient was taken as  $D_A$ . The last two boundary conditions assume infinite recombination rates.

The numerical solution of eqs 2 and 3 supports the assignment of a triangular carrier profile in P<sub>C</sub> and also determines the branching ratio between internal and external pathways for such a carrier profile. Figure 14C shows  $\bar{n}_p(\bar{x}, \bar{t})$  calculated from numerical solution of eqs 2 and 3. The reduced flux at the anode,  $\bar{j}_{sc} = d\bar{n}_p(0, \bar{t})/d\bar{x}$ , in both log-log and semilog forms, is shown in Figure 15. As with P<sub>C</sub>,  $\bar{j}_{sc}$  decays initially with near power-law behavior giving way to exponential decay at long times. Figure 16 shows the magnitude of the power-law exponent,  $a = |d(\log \bar{j}_{sc})/d(\log \bar{t})|$ , as a function of time. Early on, a value of  $1/2$  is observed, but most of the decay is characterized by a slightly larger value consistent with 0.64–0.66 observed for P<sub>C</sub> in the low-voltage region (see Figure 7). This slightly larger  $a$  is characteristic of an initially triangular carrier profile as assigned for P<sub>C</sub>. Integration of  $\bar{j}_{sc}$  in Figure 15 yielded two-thirds of the initial stored charge, as assumed above in calculating  $C_{dl}$ .

The initial value of  $a = 1/2$  and its increase with time is expected from classic electrochemical experiments. The short-circuit experiment bears analogy to the Cottrell experiment in more conventional three-electrode electrochemical cells.<sup>47</sup> The Cottrell experiment is based on driving to zero the surface

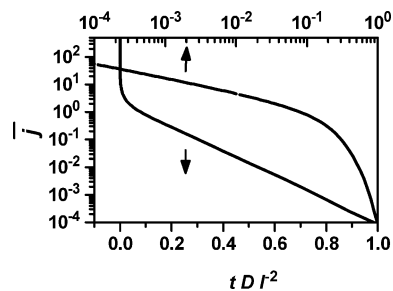


**Figure 15.** Decay from steady state from numerical simulations using eqs 2 and 3, plotted as the reduced flux at the anode,  $\bar{j}_{sc} = d\bar{n}_p(0, \bar{t})/d\bar{x}$ , as a function of  $\bar{t}$ . The reduced flux is plotted in both log-log and semilog forms to illustrate the crossover from power-law to exponential behavior.

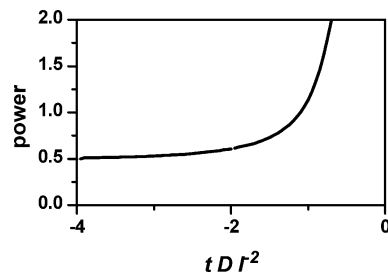


**Figure 16.** The power  $a = |d(\log \bar{j}_{sc})/d(\log \bar{t})|$  as a function of  $\bar{t}$  from numerical simulations of eqs 2 and 3. At very early times,  $a = 1/2$  is observed, similar to the power law expected for the Cottrell experiment. As time progresses,  $a$  increases to slightly greater than  $1/2$ . The sharp increase in the apparent power at long times represents the transition to the exponential dependence, as shown in Figure 15.

concentration of a redox species in a semi-infinite solution of initially constant concentration  $n_0$ . An analytic solution for the Cottrell experiment is available and predicts a  $t^{-1/2}$  dependence.<sup>47</sup> The short-circuit experiment herein is similar except that the initial profile is triangular rather than a constant concentration. At the earliest times, the profile is only perturbed over a very small fraction of  $l$ , and hence, it is effectively constant, leading to  $a = 1/2$ . As the profile extends from the anode, the triangular profile results in a slightly stronger dependence of the gradient in the carrier concentration near the anode with time and an increase in  $a$ . The Cottrell experiment provides a ready means of extracting the product  $D^{1/2}n_0$ , for instance, from the log  $J$ -intercept of a log  $J$ -log  $t$  plot. The more complex decay in the case of a triangular initial condition somewhat complicates an analogous extraction of  $D_A^{1/2}n_p(0, 0)$ .<sup>53</sup>

The anion diffusion coefficient can be more clearly extracted from the long-time exponential decay. The onset of the exponential decay signals interaction with the cathode. The carrier profile becomes symmetric, and the external and internal pathways are balanced. This situation is analogous to a potential step in a two-electrode, thin-layer electrochemical cell where an analytical solution is available.<sup>47</sup> The decay in this case goes as  $\exp(-\pi^2\bar{t})$ . Indeed, the reduced time constant extracted from a fit to the long- $\bar{t}$  portion of the numerical solution to eqs 2 and 3 is  $1/\pi^2$ . The  $D_A$  extracted for film PC1 was  $3 \times 10^{-11} \text{ cm}^2 \text{ s}^{-1}$  and was in this range for all of the films studied. Again, this value may be influenced by residual DMSO within the films.

The diffusion coefficient extracted from  $J_{sc}$  is more than that extracted from the conductivity, assuming a pseudo-free-carrier model and that the density of free ions is equal to the stoichiometric ion concentration. The ionic conductivity from the slope of the fast  $J$ - $V_{app}$  curve of PC1 is  $2 \times 10^{-8} \Omega^{-1} \text{ cm}^{-1}$ . This leads to a mobility  $\mu_A = 7.0 \times 10^{-11} \text{ cm}^2 \text{ s}^{-1}$  from  $\sigma = n_A q \mu_A$ . Assuming the validity of the Einstein relation then



leads to  $D_A^\sigma = 1.7 \times 10^{-12} \text{ cm}^2 \text{ s}^{-1}$ , an order of magnitude lower than  $D_A = 3 \times 10^{-11} \text{ cm}^2 \text{ s}^{-1}$ . The discrepancy, as with the comparison between  $C_{\text{dl}}$  and  $C_{\text{dl}}^{\text{GC}}$ , again suggests that the density of free ions is much lower than the stoichiometric ion density in  $\text{Pc}$ , owing to strong ion pairing.

Up to now, the form of  $J_{\text{ss}}$  has not been discussed. The current in the low-voltage, predominately diffusive regime is expected to be given by Fick's first law

$$J_{\text{ss}} = -qD_p \frac{dn_p}{dx} \quad (4)$$

For the triangular profile of Figure 14A, the carrier gradient is given by

$$\frac{dn_p}{dx} = -\frac{n_p(0, \text{ss})}{l} \quad (5)$$

The triangular profile along with the branching ratio discussed above also permit  $n_p(0, \text{ss})$  to be calculated from  $Q_{\text{sc}}$ :  $n_p(0, \text{ss}) = 3Q_{\text{sc}}/ql$ . This relation applied to the data of Figure 8 yields  $n_p(0, \text{ss})$  increasing linearly from  $0.7 \times 10^{18} \text{ cm}^{-3}$  to  $2 \times 10^{18} \text{ cm}^{-3}$  as  $V_o$  increases from 0.5 to 1.0 V for PC1. This linear increase predicts that  $J_{\text{ss}}$  should also increase linearly with voltage. In contrast,  $J_{\text{ss}}$  is observed to increase more rapidly. The magnitude of the nonlinearity is evidenced by calculation of the diffusion coefficient from  $J_{\text{sc}}$  and  $Q_{\text{sc}}$  according to eqs 4 and 5, which yields  $D_p$  increasing from  $1.8 \times 10^{-8}$  to  $3.1 \times 10^{-8} \text{ cm}^2 \text{ s}^{-1}$  over the voltage range 0.5–1.0 V for PC1. The increase in the calculated value of  $D_p$  resulting from the nonlinearity of the  $J_{\text{ss}}-V_{\text{app}}$  relation points to some fundamental inadequacy of the simple model presented above. Nevertheless, we deem the calculated value of  $D_p$  to be a rough estimate of the true hole diffusion coefficient. Analysis of four separate samples in the low-voltage regime with thicknesses near 300 nm yielded values of  $D_p$  in the range  $(1-8) \times 10^{-8} \text{ cm}^2 \text{ s}^{-2}$ . This value is similar to the carrier diffusion coefficients reported in redox polymers.<sup>55,56</sup>

A number of important effects neglected in the above treatment may help explain the sharper than linear increase of  $J_{\text{ss}}$  with  $V_o$  in the low-voltage regime. First, the recombination point will move from the cathode as the voltage increases. As the cathode double layer continues to change,  $n_n(l, \text{ss})$  will increase exponentially and will eventually overtake the charge stored in the double layer. The system will begin transitioning from the unipolar case to the bipolar case. As  $n_n(l, \text{ss})$  continues to rise, the recombination point will move from the cathode into the bulk of the film. An infinite recombination rate will result in the hole and electron concentrations decaying linearly to the recombination point at a distance  $x_p$  from the anode and a distance  $x_n$  from the cathode, as shown in Figure 17A. The position of the recombination point will be determined by the relative diffusivities of the two carriers,<sup>54</sup> as the continuity of the current will require that  $D_n dn_n/dx = -D_p dn_p/dx$ . As the system transitions from the unipolar case to the bipolar case, the change in  $x_p$  will cause  $J_{\text{ss}}$  to increase more rapidly than  $Q_{\text{sc}}$ , because  $J_{\text{ss}} \propto n_p(0, \text{ss})/x_p$ , whereas  $Q_{\text{sc}} \propto n_p(0, \text{ss}) x_p$ . A second effect that may need to be considered is a finite recombination rate either at the cathode or with electrons in the polymer film. Finally, any nonuniformity in film thickness may result in a distribution of transport pathways leading to more complex  $J_{\text{ss}}-V_{\text{app}}$  behavior. Numerical modeling is currently being pursued to better understand the signatures of the first two effects.

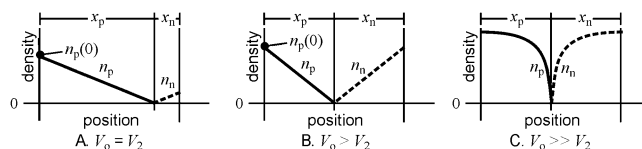


**Figure 17.** Plots of hole (solid line) and electron (dashed line) density vs position as the system transitions from the low- to high-voltage regime. (a) Profiles for  $V_o = V_2$  near the onset of the high-voltage regime. The injection of holes and electrons is asymmetric, and both densities decay linearly to the recombination point a distance  $x_p$  from the anode and  $x_n$  from the cathode. (B) At  $V_o > V_2$ , the injection of holes and electrons becomes more symmetric. There is still no significant field within the device, and consequently, the carrier profiles are linear. (C) At  $V_o \gg V_2$ , a field exists within  $\text{Pc}$  that causes the doped regions to grow into the film and become more uniform.

**Steady State, High-Voltage Regime.** The high-voltage regime is characterized by the following major observations: (1)  $J_{\text{ss}}$  decreases with increasing  $l$ ; (2)  $V_{\text{oc}}^\circ$  is a nearly constant value and less than  $V_o$ ; (3)  $Q_{\text{sc}}$  increases linearly with  $V_o$  and more rapidly than in the low-voltage regime; (4)  $J_{\text{sc}}$  decays from steady state following a near- $t^{-0.5}$  power law; (5)  $J_{\text{ss}}$  increases nonlinearly with  $V_o$ .

The transition from the low- to high-voltage regime is marked by the onset of bipolar injection. The sharp increase in  $Q_{\text{sc}}$  versus  $V_{\text{app}}$  is consistent with substantial bipolar injection. Unlike with the non-Faradaically-controlled charging discussed above, the injection of both electrons and holes can preserve both local and global charge neutrality. Consequently, it is possible for a much larger density of charge to be injected into the polymer film. The system now begins to resemble the Faradaic charging of a battery,<sup>57</sup> but with interpenetrating ionic and electronic pathways. Substantial charging of the battery occurs when  $V_o$  approaches the standard potential required for disproportionation or  $|E_{\text{p/u}}^\circ - E_{\text{n/n}}^\circ| = 1.4 \text{ V}$ . At the highest  $V_o$  investigated, sufficient redox chemistry has occurred to become evident by UV-vis spectroscopy. Separate three-electrode spectroelectrochemical experiments demonstrate that our experimental apparatus can detect doping only at average levels in excess of  $1 \times 10^{19} \text{ cm}^{-3}$ . Above,  $n_p(0, \text{ss})$  was estimated to be  $2 \times 10^{18} \text{ cm}^{-3}$  at 1 V. Hence, it is consistent that the onset of observed spectral changes (see Figure 12) occurred at  $\sim 3 \text{ V}$ , where  $Q_{\text{sc}}$  is a factor of 4 larger. This also supports the notion that  $Q_{\text{sc}}$  is indeed measuring a significant fraction of the charge stored in the polymer.

Initially, it might be expected that the density of injected charge in the high-voltage, bipolar regime would increase exponentially with applied bias according to the Nernst equation. Of course, this will only be the case as long as the density of injected charge remains less than  $n_u$  such that  $n_u \approx n_{\text{tot}}$ , and as long as the ion distribution is not too strongly affected. As the density of injected charge increases, not all of the applied bias will drive an increase in the doping level, but an increasing fraction will be needed to maintain the gradient in ion concentration required for local charge neutrality. In other words, a substantial electric field will begin to develop across the sample and can influence the transport of electronic carriers. In the case of polymer light-emitting electrochemical cells (LECs), electric fields within the polymer film have been postulated to exist after the onset of doping because of recombination of the injected carriers.<sup>2,3,32,34,58-61</sup>

For reasons discussed above, the divergence of  $V_{\text{app}}$  and  $V_{\text{oc}}^\circ$  is evidence for just such a field driving the migration of electronic carriers. This suggests that, in the high-voltage regime, the density of injected charge approaches that of the anion density. At 1 V, the density of injected charge is approximately



$5 \mu\text{C cm}^{-2}$ , which with a triangular carrier profile translates to  $n_p(\text{anode, ss}) = 2 \times 10^{18} \text{ cm}^{-3}$ . This is still substantially less than the stoichiometric ion density of  $1.8 \times 10^{21} \text{ cm}^{-3}$ , but together with  $C_{\text{dl}} \ll C_{\text{dl}}^{\text{GC}}$ , adds to the evidence that the effective free-ion density is on the order of  $10^{18}$ – $10^{19} \text{ cm}^{-3}$ .

The presence of an electric field in the bulk is expected to alter the shape of the steady-state carrier densities. In the absence of a field and neglecting recombination, the continuity equation (Fick's second law) requires that the carrier profiles decay linearly from the electrode to the recombination region. In the presence of a field, however, the carrier profiles can now be driven deeper into the sample, as shown in Figure 17C.<sup>34</sup> The gradient in the steady-state carrier densities in the recombination-free zones decreases, as migration can support the current. The system approaches two uniformly doped regions meeting at the recombination zone, as shown in Figure 17C.

The transition of  $a$  from  $\sim 0.65$  in the low-voltage regime to  $\sim 0.5$  in the high-voltage regime (see Figure 7) supports the formation of regions of more uniform doping level. The  $1/2$  power is characteristic of an electrode reaction depleting an initially uniform concentration of redox sites as in the Cottrell experiment. The symmetry of the carrier density is expected to now result in a branching ratio of 0.5 between the external and internal pathways and consequently the true density of injected charge being  $1/2$  the total charge. Note that  $Q_{\text{sc}}$  measures the density of charge stored in p-type states equal to the density stored in n-type states in the limit that  $Q_{\text{dl}}$  can be neglected.

The decay of  $V_{\text{oc}}$  also supports the formation of more uniformly doped regions. In the high-voltage regime,  $V_{\text{oc}}$  primarily measures the difference in chemical potential of  $\text{P}_C$  between the anode and cathode surfaces. The region of nearly constant  $V_{\text{oc}}$  (Figure 9a) signifies a period of time over which the doping level at the anode and cathode surfaces remains unchanged. In the open-circuit experiment, the decay of the system will occur from the recombination zone outward. Any substantial region of uniform doping extending from the electrode surfaces will shield the surface doping levels from changes in the recombination zone and hence preserve  $V_{\text{oc}}$  near a constant value for some time.

Although the growth of doped regions into the sample begins to resemble a pn junction, the steady-state current appears to remain controlled by the bulk processes. The transient characterization of the steady state in the high-voltage regime reveals rectifying  $J$ – $V_{\text{app}}$  characteristics reminiscent of a pn junction (see Figure 10). The fact that the transient  $J$ – $V_{\text{app}}$  characteristics are not exponential suggests that the  $J$ – $V_{\text{app}}$  characteristics do not follow the mechanisms observed in inorganic semiconductor pn junctions. The near-linearity of the transient  $J$ – $V_{\text{app}}$  characteristics in the vicinity of  $V_o$  indicates that the steady-state current is controlled by bulk transport through the doped regions rather than by recombination processes at the junction between the p- and n-type regions. The near-linearity also indicates that the Au contacts behave ohmically over the current ranges investigated. The asymmetric  $J$ – $V_{\text{app}}$  characteristics can be explained by considering the carrier densities within the polymer film immediately after the applied voltage is removed. At this point, the injected electrons and holes will begin to recombine, forming a transient in situ pn junction within the polymer film. This junction will impede the flow of current through the polymer film until a voltage greater than the transient built-in voltage of the junction is applied. This transient built-in voltage is the  $V_{\text{oc}}$  extracted from the transient  $J$ – $V_{\text{app}}$  characteristics. Then, for applied voltages greater than  $V_{\text{oc}}$ , the  $J$ – $V_{\text{app}}$  characteristics are essentially linear, behaving as a resistor.

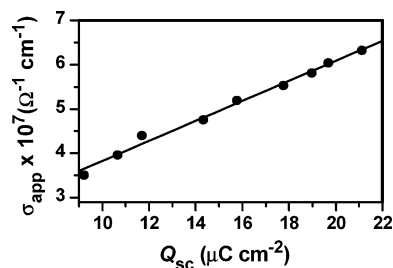


**Figure 18.** The apparent conductivity ( $\sigma_a$ ) as a function of  $Q_{\text{sc}}$ . The  $\sigma_a$ 's were measured from the highly conducting portions of the transient  $J$ – $V_{\text{app}}$  measurements of Figure 10 (PC1,  $l = 300 \text{ nm}$ ). The black line is the best-fit line to the values in the high-voltage regime. The slope of this line was used to calculate an effective mobility ( $\bar{\mu}$ ) of  $9.2 \times 10^{-8} \text{ cm}^2 \text{ V}^{-1} \text{ s}^{-1}$ .

The apparent conductivity,  $\sigma_a = l(dJ/dV_{\text{app}})$ , extracted from the slope of the transient  $J$ – $V_{\text{app}}$  behavior in the vicinity of  $V_o$  is believed to be a measure of the conductance of the doped regions. The conductance of these doped regions is expected to depend on the density of the injected charge. Indeed,  $\sigma_a$  scales linearly with  $Q_{\text{sc}}$  in the high-voltage regime, as shown in Figure 18.  $J_{\text{ss}}$  increases roughly as the square of the voltage because of the combined influence of an increase in the driving field and an increase in the conductivity of the doped regions due to the injected charge.

The  $\sigma_a$  value from the transient  $J$ – $V_{\text{app}}$  characteristics can also be used to make a rough estimate of the effective carrier mobility. In the crude picture in which the carrier densities have constant values within the n- and p-type regions,  $n_o$  and  $p_o$ , respectively, the fields within these regions must also take on constant values,  $F_n$  and  $F_p$ , respectively, by continuity of the current. The field driving carrier transport is that generated by the voltage in excess of that needed to support the formation of the pn junction, crudely, that in excess of  $V_{\text{oc}}^o$ , as plotted in Figure 11. This voltage will divide across the doped regions and the recombination zone.<sup>34</sup> Neglecting the voltage drop across the recombination zone, the transient current–voltage behavior in the linear region can be written within a quasi-free-particle picture as

$$J = q(n_o + p_o)\bar{\mu} \frac{(V_o - V_{\text{oc}}^o)}{l} \quad (6)$$

where  $\bar{\mu}$  is an effective mobility

$$\bar{\mu} = \frac{\mu_n \mu_p}{\mu_n + \mu_p} \quad (7)$$

Equation 8 also assumes that  $Q_n = Q_p$ , as expected in the high-voltage regime where the charge stored in the doped states exceeds that stored in the double layer. Equation 8 can be rewritten in terms of  $Q = Q_n = Q_p = 2Q_{\text{sc}}$  and  $\sigma_{\text{app}}$  as

$$\sigma_{\text{app}} = \frac{8Q_{\text{sc}}\bar{\mu}}{l} \quad (8)$$

The slope of Figure 19 yields  $\bar{\mu} = 9.2 \times 10^{-8} \text{ cm}^2 \text{ V}^{-1} \text{ s}^{-1}$ . Any component of  $V_o - V_{\text{oc}}^o$  that drops across the recombination zone would make the calculated mobility higher.

The effective mobility  $\bar{\mu}$  calculated in the high-voltage regime is less than the hole mobility calculated in the low-voltage regime, invoking the Einstein relation ( $\mu_h = q(k_B T)^{-1} D_h = 8 \times 10^{-7} \text{ cm}^2 \text{ V}^{-1} \text{ s}^{-1}$ ). Taken at face value, this discrepancy

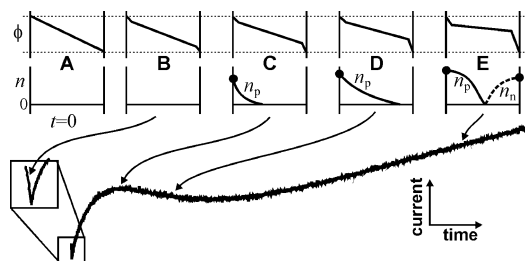


**Figure 19.** Schematic of the electrostatic potential ( $\phi$ ), and hole and electron carrier densities ( $n_p$  and  $n_n$ , respectively) at various points along a chronoamperogram collected in response to a potential step ( $V_0 = 1.5$  V).

suggests that the electron mobility is less than the hole mobility, which is typical of many organic materials. It is also consistent with dual-electrode voltammetry measurements demonstrating that the conductivity of p-PC is an order of magnitude greater than n-PC at similar doping levels.<sup>23</sup> Owing to the severity of the approximations used in estimating  $\bar{\mu}$ , in particular, neglecting any component of  $V_0 - V_{oc}^{\circ}$  that drops across the recombination zone, we prefer, however, to simply state that the electron and hole mobilities are on the order of  $10^{-7}$ – $10^{-6}$  cm<sup>2</sup> V<sup>-1</sup> s<sup>-1</sup>. It is notable that the mobility/diffusivity values calculated in very different regimes (low-voltage diffusive vs high-voltage migratory) yield similar values.

**Approach to Steady State.** The discussion above provides a framework for discussing the chronoamperograms of Figure 3 which show the approach to steady state. We provide only a qualitative discussion of the observed behavior as schematized in Figure 19. The quantitative analysis of the chronoamperograms is beyond the scope of this paper, as it is more complex than, for instance, the short-circuit decays because of contributions from both migratory and diffusive processes.

The application of bias will first result in charging the geometric capacitance of the system with the potential dropping linearly across the film as shown at the  $t = 0$  point in Figure 19A. This process occurs within 10  $\mu$ s and is essentially instantaneous on the time scale of the measurements in Figure 3. The applied bias will then induce the motion of ions and the charging of the ionic double layer (Figure 19B). As this initial charging is from migratory transport, an exponential decay is expected, and the initial 50 ms of the decay is indeed consistent with an exponential decay. As the double layers are formed, the potential difference between the gold electrode and the polymer film begins to grow, driving up the surface concentrations  $n_p(0, t)$  and  $n_n(l, t)$ . Because of the absolute potential of the gold electrode in relation to the electronic structure of PC, the surface concentration  $n_p(0, t)$  is more substantial than  $n_n(l, t)$ . The increase in surface concentration begins to drive the growth of doped regions into the film (Figure 19C). This increases the capacitance of, in particular, the anode which slows the increase of  $n_p(0, t)$  and results in a larger potential drop forming at the cathode. The p-doping at the anode side and the transport of charges through the film begin to contribute to the current.

The contribution from the doping process is very much like the current observed in standard three-electrode electrochemical experiments such as cyclic voltammetry. Focusing on the anode, we see two things changing simultaneously with time. First, the surface concentration  $n_p(0, t)$  is increasing, but at a rate that slows with time as it approaches its steady-state value. The increase in surface concentration drives an increase in the gradient of  $n_p$  at the anode surface, thereby working to increase the diffusive current. At the same time, however, the p-doped

sites extend into the film, driving a decrease in the gradient in  $n_p$  at the anode surface and thereby decreasing the diffusive current (compare Figure 19C and 19D). The combination of these two effects gives rise to the peak in the chronoamperograms observed for PC at  $t \approx 10$  s. This peak is not observed at the lowest biases, because the current from doping is too small. The observation of a peak in the potential-step experiment is quite analogous to that seen in other diffusively controlled electrochemical experiments. For instance, a peak is observed in the cyclic voltammetry of liquid redox couples because of the competition between an increasing surface concentration, as driven by the potential sweep, and the growth of the relevant concentration profile into the bulk of the solution.

At the higher voltages, the current transients for PC increase again after the peak because of the onset of n-type doping at the cathode. The increase in p-doping at the anode drives an increasing potential drop at the cathode, because it is coupled to the charging of its double layer. Eventually, this potential drop becomes sufficient to drive the n-doping of the film (Figure 19E). This adds an additional contribution to the current from the charge both stored in the doped states and transported through the film. This final increase occurs after the initial p-doping process, after approximately  $t = 25$  s for PC.

## Summary and Conclusions

There are two dominant regimes of steady-state transport in the Au | PC | Au system. At low voltages, the steady-state current is controlled by the diffusive transport of holes. The density of the injected charge remains sufficiently low that the redistribution of anions can keep the electric field in the bulk negligible. The applied bias increases the surface concentration of holes at the anode which decays linearly to zero at the cathode. Evidence for this triangular concentration profile comes from the  $t^{-0.65}$  power-law decay from steady state of the current measured through an external short circuit. The overall number and anode surface density of p-doped sites is controlled by the non-Faradaic charging of an ionic double layer at the cathode, where the majority of the applied bias drops. The asymmetry in the potential drop results from the difference in the charge–voltage relation for n-type versus p-type doping due to the position of the metal Fermi level relative to  $E_{p/u}^{\circ}$  and  $E_{u/n}^{\circ}$ . The ionic double-layer charging capacitance is 5  $\mu$ F cm<sup>-2</sup>, the value of which suggests an effective anion density much lower than the stoichiometric density of anions in the film. The hole diffusion coefficient from  $J_{ss}$  and  $Q_{sc}$  under the assumption of a simple triangular carrier profile is estimated to be on the order of  $D_p = 10^{-8}$  cm<sup>2</sup> s<sup>-1</sup>.

The crossover from the low-voltage to high-voltage regime is marked by the onset of substantial bipolar injection. The overall density of stored charge increases more rapidly with applied bias than in the low-voltage regime. Unlike the non-Faradaically-controlled charging in the low-voltage regime, the Faradaic charging in the high-voltage regime can permit more substantial n- and p-type doping, because both local and global charge neutrality is preserved. This crossover occurs at a  $V_0$  of  $\sim 1.4$  V, which happens to coincide with the band gap of the polymer ( $E_{p/u}^{\circ} - E_{u/n}^{\circ}$ ). The increased density of doped sites begins to perturb the anion distribution to a sufficient extent that carrier transport crosses over from diffusive to migratory. The carrier profiles begin to more closely approximate two uniformly doped regions (one p-type and one n-type) meeting at some recombination zone. Evidence for more uniform carrier profiles comes from the  $t^{-0.5}$  current decay of the steady-state system under short-circuit conditions and the initial period of

nearly constant voltage for decay under open-circuit conditions. The steady-state current in the high-voltage regime is governed by bulk transport of carriers through the n- and p-type regions by migration. Evidence for electric-field-driven transport comes from the divergence of the open-circuit voltage from the applied bias. Evidence for a bulklike transport process comes from transient current–voltage characterization that shows linear behavior in the vicinity of the steady state. The steady-state current increases nonlinearly because of both an increase in the driving field and an increase in the conductivity of the doped regions due to injected charge. A crude estimate of the effective mobility,  $\bar{\mu} = 10^{-7} \text{ cm}^2 \text{ V}^{-1} \text{ s}^{-1}$ , is on the order of the hole diffusion coefficient calculated in the low-voltage regime and indicates that the hole and electron mobilities are on the order of  $10^{-7}$ – $10^{-6} \text{ cm}^2 \text{ V}^{-1} \text{ s}^{-1}$ .

**Acknowledgment.** This work was supported by NSF-DMR 0210078. C.H.W. Cheng thanks the NSF Integrative Graduate Education and Research Training (IGERT) program at the University of Oregon for support.

## References and Notes

- (1) deMello, J. C.; Tessler, N.; Graham, S. C.; Friend, R. H. *Phys. Rev. B* **1998**, *57*, 12951.
- (2) Pei, Q.; Yang, Y.; Yu, G.; Zhang, C.; Heeger, A. J. *J. Am. Chem. Soc.* **1996**, *118*, 3922.
- (3) Pei, Q.; Yu, G.; Zhang, C.; Yang, Y.; Heeger, A. J. *Science* **1995**, *269*, 1086.
- (4) Edman, L.; Pauchard, M.; Moses, D.; Heeger, A. J. *J. Appl. Phys.* **2004**, *95*, 4357.
- (5) Gao, J.; Dane, J. *Appl. Phys. Lett.* **2003**, *83*, 3027.
- (6) Rudmann, H.; Rubner, M. F. *J. Appl. Phys.* **2001**, *90*, 4338.
- (7) Maness, K. M.; Terrill, R. H.; Meyer, T. J.; Murray, R. W.; Wightman, R. M. *J. Am. Chem. Soc.* **1996**, *118*, 10609.
- (8) Gao, J.; Yu, G.; Heeger, A. J. *Adv. Mater.* **1998**, *10*, 692.
- (9) Chen, X. L.; Bao, Z.; Schon, J. H.; Lovinger, A. J.; Li, Y.-Y.; Crone, B.; Dodabalapur, A.; Batlogg, B. *Appl. Phys. Lett.* **2001**, *78*, 228.
- (10) Kittleson, G. P.; White, H. S.; Wrighton, M. S. *J. Am. Chem. Soc.* **1985**, *107*, 7373.
- (11) Ofer, D.; Crooks, R. M.; Wrighton, M. S. *J. Am. Chem. Soc.* **1990**, *112*, 7869.
- (12) Nilsson, D.; Chen, M.; Kugler, T.; Remonen, T.; Armgarth, M.; Berggren, M. *Adv. Mater.* **2002**, *14*, 51.
- (13) Thackeray, J. W.; White, H. S.; Wrighton, M. S. *J. Phys. Chem.* **1985**, *89*, 5133.
- (14) Bulovic, V.; Mandell, A.; Perlman, A. Molecular Memory Device. *U. S. Pat. Appl.* **2004**, 11.
- (15) Bulovic, V.; Mandell, A.; Perlman, A. Addressable and electrically reversible memory switch. *U. S. Pat. Appl. Publ.* **2004**, 11.
- (16) Chen, M.; Nilsson, D.; Kugler, T.; Berggren, M.; Remonen, T. *Appl. Phys. Lett.* **2002**, *81*, 2011.
- (17) Abruna, H. D.; Denisevich, P.; Umana, M.; Meyer, T. J.; Murray, R. W. *J. Am. Chem. Soc.* **1981**, *103*, 1.
- (18) Denisevich, P.; Willman, K. W.; Murray, R. W. *J. Am. Chem. Soc.* **1981**, *103*, 4727.
- (19) Pickup, P. G.; Leidner, C. R.; Denisevich, P.; Murray, R. W. *J. Electroanal. Chem.* **1984**, *164*, 39.
- (20) Pickup, P. G.; Murray, R. W. *J. Electrochem. Soc.* **1984**, *131*, 833.
- (21) Pickup, P. G.; Kutner, W.; Leidner, C. R.; Murray, R. W. *J. Am. Chem. Soc.* **1984**, *106*, 1991.
- (22) Langsdorf, B. L.; Zhou, X.; Adler, D. H.; Lonergan, M. C. *Macromolecules* **1999**, *32*, 2796.
- (23) Lonergan, M. C.; Cheng, C. H.; Langsdorf, B. L.; Zhou, X. *J. Am. Chem. Soc.* **2002**, *124*, 690.
- (24) Cheng, C. H. W.; Boettcher, S. W.; Johnston, D. H.; Lonergan, M. C. *J. Am. Chem. Soc.* **2004**, *126*, 8666.
- (25) Cheng, C. H. W.; Lonergan, M. C. *J. Am. Chem. Soc.* **2004**, *126*, 10536.
- (26) Langsdorf, B. L.; Zhou, X.; Lonergan, M. C. *Macromolecules* **2001**, *34*, 2450.
- (27) Kaufman, J. H.; Chung, T.-C.; Heeger, A. J. *J. Electrochem. Soc.* **1984**, *131*, 2847.
- (28) The time resolution of the experiment was not sufficient to capture the initial rise in current due to the RC charging of the circuit. Separate impedance measurements yield a geometric capacitance of  $10 \text{ nF cm}^{-2}$  for the system and an RC time constant of 1 ms.
- (29) de Mello, J. C. *Phys. Rev. B* **2002**, *66*, 235210/1.
- (30) Manzanares, J. A.; Riess, H.; Heeger, A. J. *J. Phys. Chem. B* **1998**, *102*, 4327.
- (31) Riess, I.; Cahen, D. *J. Appl. Phys.* **1997**, *82*, 3147.
- (32) Rudmann, H.; Shimada, S.; Rubner, M. F. *J. Appl. Phys.* **2003**, *94*, 115.
- (33) Sampietro, M.; Sotgiu, R.; Wenzl, F. P.; Holzer, L.; Tasch, S.; Leising, G. *Phys. Rev. B* **2000**, *61*, 266.
- (34) Smith, D. L. *J. Appl. Phys.* **1997**, *81*, 2869.
- (35) Buda, M.; Kalyuzhny, G.; Bard, A. J. *J. Am. Chem. Soc.* **2002**, *124*, 6090.
- (36) Edman, L.; Summers, M. A.; Buratto, S. K.; Heeger, A. J. *Phys. Rev. B* **2004**, *70*, 115212/1.
- (37) Buck, R. P. *J. Phys. Chem.* **1988**, *92*, 4196.
- (38) Buck, R. P. *J. Phys. Chem.* **1988**, *92*, 6445.
- (39) Buck, R. P. *J. Electroanal. Chem.* **1989**, *271*, 1.
- (40) Chen, K.; Shriver, D. F. *Chem. Mater.* **1991**, *3*, 771.
- (41) Ganapathiappan, S.; Chen, K.; Shriver, D. F. *J. Am. Chem. Soc.* **1989**, *111*, 4091.
- (42) Doan, K. E.; Ratner, M. A.; Shriver, D. F. *Chem. Mater.* **1991**, *3*, 418.
- (43) Jacobs, P. W. M.; Lorimer, J. W.; Russer, A.; Wasiucionek, M. *J. Power Sources* **1989**, *26*, 503.
- (44) Vallee, A.; Besner, S.; Prud'homme, J. *Electrochim. Acta* **1992**, *37*, 1579.
- (45) Zahurak, S. M.; Kaplan, M. L.; Rietman, E. A.; Murphy, D. W.; Cava, R. J. *Macromolecules* **1988**, *21*, 654.
- (46) Ratner, M. A.; Shriver, D. F. *Chem. Rev.* **1988**, *88*, 109.
- (47) Bard, A. J.; Faulkner, L. R. *Electrochemical Methods*; John Wiley & Sons: New York, 1980.
- (48) Buck, R. P. *J. Electroanal. Chem.* **1986**, *210*, 1.
- (49) In non-MIECs, the observation of a thickness dependence can be consistent with interfacial processes limiting charge transport as in the case of Fowler–Nordheim tunneling in a metal | insulator | metal system.
- (50) This is referring only to the electronic carriers. For instance, the double-layer charges refer to the excess electrons or holes on the surface of the metal electrodes, which are balanced by ionic charges within the polymer film. Similarly, the electrons or holes stored in doped states are balanced by ions within the polymer sample.
- (51) The average charge density in the film is on the order of  $10^{18} \text{ cm}^{-3}$  as compared to  $n_{\text{tot}} \approx 5 \times 10^{20} \text{ cm}^{-3}$ .
- (52) Rep, D. B. A.; Morpurgo, A. F.; Sloof, W. G.; Klapwijk, T. M. *J. Appl. Phys.* **2003**, *93*, 2082.
- (53) Applying the Cottrell expression to a fit of the log–log plot shown in Figure 17 over the reduced time range of  $5 \times 10^{-4}$  to  $5 \times 10^{-2}$  yields a factor of 3 overestimation of the diffusion coefficient and power of 0.59. Applying this approach to the experimental data for  $P_C$  over the range  $t = 0.01$ – $1$  s and using  $^{3/2}Q_{\text{sc}} = Q_p = n_p(0, 0)^{1/2}$  yields  $D_A = 4 \times 10^{-11} \text{ cm}^2 \text{ s}^{-1}$ .
- (54) Pichot, F.; Bloom, C. J.; Rider, L. S.; Elliott, C. M. *J. Phys. Chem. B* **1998**, *102*, 3523.
- (55) Dalton, E. F.; Surridge, N. A.; Jernigan, J. C.; Wilbourn, K. O.; Facci, J. S.; Murray, R. W. *Chem. Phys.* **1990**, *141*, 143.
- (56) Terrill, R. H.; Murray, R. W. *Mol. Electron.* **1997** **1997**, 215.
- (57) Buck, R. P.; Surridge, N. A.; Murray, R. W. *J. Electrochem. Soc.* **1992**, *139*, 136.
- (58) deMello, J. C.; Halls, J. J. M.; Graham, S. C.; Tessler, N.; Friend, R. H. *Phys. Rev. Lett.* **2000**, *85*, 421.
- (59) Dick, D. J.; Heeger, A. J.; Yang, Y.; Pei, Q. *Adv. Mater.* **1996**, *8*, 985.
- (60) Gao, J.; Heeger, A. J.; Campbell, I. H.; Smith, D. L. *Phys. Rev. B* **1999**, *59*, R2482.
- (61) Gao, J.; Dane, J. *Appl. Phys. Lett.* **2004**, *84*, 2778.